Joule

Article

Diagnostic-free onboard battery health assessment

Graphical abstract

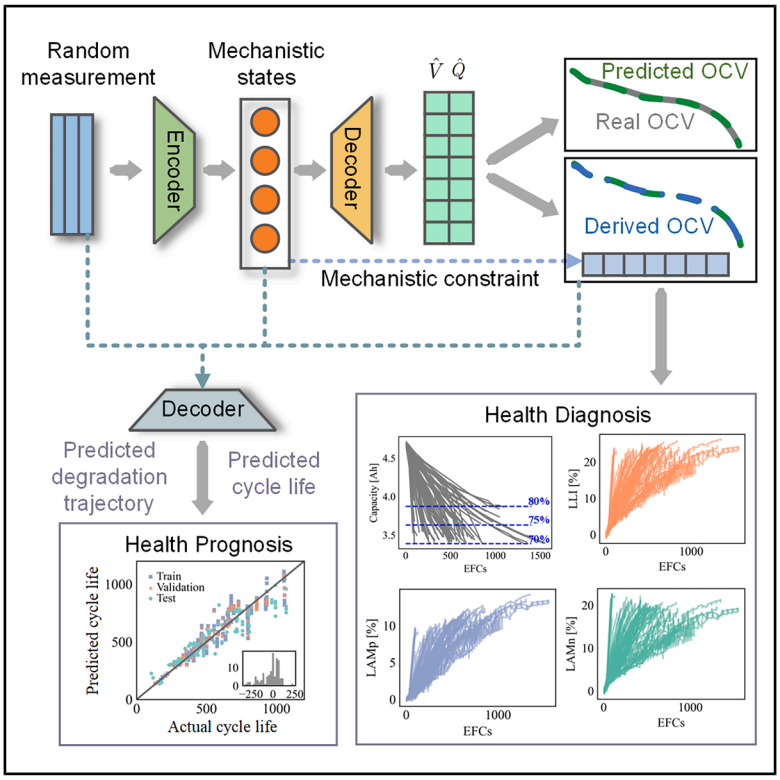

Highlights

- Onboard battery health assessment without diagnostic tests and historical data
- Physics-constrained interpretable model for understanding aging mechanisms
- Adaptive to random portions of operational measurements and dynamic loadings
- Flexible for different application interests across the full lifespan

Authors

Yunhong Che, Vivek N. Lam, Jinwook Rhyu, ..., Martin Z. Bazant, William C. Chueh, Richard D. Braatz

Correspondence

braatz@mit.edu

In brief

An interpretable machine learning model is proposed to enable rapid, onboard battery health assessment by only using portions of operational measurements from charging or dynamic discharging without diagnostic tests. The degradation path is reconstructed with mechanisms tracking, and the future degradation trajectory and cycle life are predicted during onboard operations.

Che et al., 2025, Joule *9*, 102010
August 20, 2025
https://doi.org/10.1016/j.joule.2025.102010

CellPress

Please cite this article in press as: Che et al., Diagnostic-free onboard battery health assessment, Joule (2025), https://doi.org/10.1016/j.joule.2025.102010

Joule

CellPress

Article

Diagnostic-free onboard battery health assessment

Yunhong Che,[1,7] Vivek N. Lam,[2,3,7] Jinwook Rhyu,[1] Joachim Schaeffer,[1,4] Minsu Kim,[1] Martin Z. Bazant,[1,5] William C. Chueh,[2,3,6] and Richard D. Braatz[1,8,*]

[1]Department of Chemical Engineering, Massachusetts Institute of Technology, Cambridge, MA 02139, USA
[2]Department of Materials Science and Engineering, Stanford University, Stanford, CA 94305, USA
[3]Applied Energy Division, SLAC National Accelerator Laboratory, Menlo Park, CA 94025, USA
[4]Control and Cyber-Physical Systems Laboratory, Technical University of Darmstadt, Darmstadt 64283, Germany
[5]Department of Mathematics, Massachusetts Institute of Technology, Cambridge, MA 02139, USA
[6]Department of Energy Science and Engineering, Stanford University, Stanford, CA 94305, USA
[7]These authors contributed equally
[8]Lead contact
*Correspondence: braatz@mit.edu
https://doi.org/10.1016/j.joule.2025.102010

CONTEXT & SCALE Batteries degrade during usage, reducing their energy and power supply performance. Diverse usage conditions lead to complex and varying degradation mechanisms occurring inside batteries. Separate diagnostic cycles are often used to untangle the battery's current state of health from prior complex aging patterns. However, these same diagnostic cycles alter the battery's degradation trajectory, are time-intensive, and cannot be practically performed in onboard applications.

This paper presents an interpretable, diagnostic-free model for onboard battery health diagnosis and prognosis, along with an interpretation of aging mechanisms. By only using the random portions of operational measurements from the battery management system, the degradation path can be reconstructed, and the future degradation trajectory can be predicted. Electrode-level aging mechanisms are revealed, and the cycle life is forecasted during onboard operations, thus providing better guidance for predictive maintenance and battery design. This framework is effective with dynamic loadings and is flexible for different applications, including battery design and characterization, onboard management, and retirement.

SUMMARY

Diverse usage patterns induce complex and variable aging behaviors in lithium-ion batteries, complicating accurate health diagnosis and prognosis. In this work, we leverage portions of operational measurements from charging or dynamic discharging in combination with an interpretable machine learning model to enable rapid, onboard battery health diagnostics and prognostics without offline diagnostic testing and access to historical data. We integrate mechanistic constraints derived from differential voltage analysis within an encoder-decoder to extract electrode health states in a physically interpretable latent space, which enables improved reconstruction of the degradation path with onboard aging mechanisms tracking. The diagnosis model can be flexibly applied across diverse applications with slight fine-tuning. We demonstrate the model's versatility by applying it to three battery-cycling datasets consisting of 422 cells under different operating conditions, with a mean absolute error of less than 2% for health diagnosis under varying conditions, highlighting the utility of an interpretable, diagnostic-free model.

INTRODUCTION

The growing trend of electrification has driven the wide application of lithium-ion batteries in electrified transportation and grid storage.[1,2] One of the primary concerns during battery usage is degradation, leading to reduced capacity and power capabilities. Knowing a battery's current and future state of health (SOH) is critical in optimizing its usage. However, the complex path-dependent nature of battery degradation results in diverse practical degradation patterns, which pose challenges for accurate health diagnosis and prognosis.[2,3] Typically, a diagnostic cycle is employed to assess the SOH of the battery.[4–9] This diagnostic cycle may include pulse tests to check resistance, low-rate capacity checks, and other application-specific tests necessary to extract useful SOH metrics. Key information obtained from the diagnostic test is further used in other battery-related research, such as modeling and parameter identification, state estimation and

cycle life prediction, materials characterization, and second-life applications.[10–13]

One common SOH metric is the low-rate battery capacity. However, this metric alone is insufficient, as multiple degradation pathways can lead to the same cell-level SOH, limiting the interpretative power of relying solely on the cell-level capacity. To address this, electrode-specific capacities have been proposed and extensively studied as a means to further break down degradation into electrode-level phenomena, capturing the more intricate aging behavior of lithium-ion batteries.[6,7,14–16] This mechanistic model, known as differential voltage analysis (DVA), reconstructs the battery's open-circuit voltage (OCV) by subtracting matched and rescaled half-cell OCV curves. Using these half-cell curves, DVA reveals key modes of battery aging, such as loss of active materials (LAMs) and loss of lithium inventory (LLI).[17–19] Although this analysis provides valuable *in situ* insight into aging mechanisms, it is typically performed on pseudo-OCV curves at rates of C/20 or lower, taken during a diagnostic cycle. Furthermore, even at low rates, this adjustment does not fully capture the pseudo-OCV curve due to changes in half-cell overpotential, inhomogeneities of lithiation, and other aging effects.[20–22]

While diagnostic cycles provide valuable insights into the battery's SOH, such as enabling DVA, they have significant drawbacks. Taking time away from aging to perform disruptive and time-intensive diagnostic cycles can drastically alter the trajectory of battery aging.[5] From a practical point of view, time-consuming diagnostic tests cannot be performed routinely on consumer electronics, leading to the need for onboard diagnostics that use operational data. In real-world applications, battery charging current rates (C-rates), state-of-charge (SOC) ranges/voltage windows, and load profiles can vary significantly, necessitating data-driven models that are robust across diverse operating conditions.[2,23–25] Moreover, a significant number of lithium-ion batteries are expected to retire from electric vehicles (EVs) in the near future with varying conditions, but performing a lengthy diagnostic cycle to evaluate their performance will be costly.[26–28] To facilitate more intelligent repackaging and reuse, rapid evaluation of battery performance has garnered increased attention. Finally, different C-rate-based diagnostic tests are required in diverse applications, necessitating the model's suitability under varying scenarios.[29,30]

In recent years, the advanced development of machine learning models has led to their implementation in battery health estimations and predictions.[2,31–35] Data-driven predictions of the OCV curve and the incremental capacity (IC) curve have shown potential for onboard health diagnosis by using measured current and voltage.[36,37] Deep neural networks are used predominantly in these data-driven models for the prediction of the battery OCV curve or charging curve due to their good nonlinear mapping capabilities.[37–40] However, despite achieving high prediction accuracy, the input data is usually fixed to a specific voltage curve under constant current (CC) between the voltage limits. This limits generalization to real applications with partial SOC cycling or dynamic load profiles. Additionally, the "black box" nature of these models limits their interpretability for a battery engineer to better understand the failure modes of a given battery. Consequently, mechanistic models are still required for subsequent aging mechanism analysis, which is separate from machine learning.

To improve the interpretability of battery health models, promising ways of combining physical models with machine learning have been discussed.[41,42] One approach involves extracting physically interpretable features from mechanistic models to inform machine learning models used for battery modeling, health estimation, and cycle life prediction.[6,7,43,44] However, the extraction of these physical features poses challenges and typically requires specific and time-consuming diagnostic tests. Physics-informed neural networks (PINNs), which integrate governing equations from mechanistic models to constrain machine learning models, show promise in improving both interpretability and the speed of solving governing equations in complex models.[45–47] However, not only is the construction of explicit models with partial derivatives challenging, but current models also do not fully capture highly interconnected degradation processes during battery aging.[48]

Here, we propose an interpretable model for the diagnosis and prognosis of complex battery aging that can be performed without separate diagnostic tests. Instead of a diagnostic, this model uses partial operating data with random SOC windows truncated from the full charging/discharging curves that emulate the measured data from practical applications. An autoencoder integrates mechanistic states in a physically meaningful latent space, which is constructed through the DVA-based model and the alignment between the derived OCV and predicted OCV, enabling interpretable battery diagnosis and prognosis. Consequently, our model demonstrates the potential of machine learning to replace time-consuming and costly offline testing and model fitting to enhance onboard health management without requiring historical data. Furthermore, by fine-tuning our model, we demonstrate the swift transferability to different applications. We evaluate the model for three datasets: the van Vlijmen et al.[6] dataset, which comprises 236 batteries sourced from a Tesla Model 3 cycled under 126 different CC operating conditions; the Geslin et al.[7] dataset, which comprises 92 batteries under both constant and dynamic cycling conditions; and a new dataset consisting of a subset of 94 batteries from the van Vlijmen et al. dataset that underwent further low-rate (such as C/80 and C/40) validation tests. These exemplary use cases demonstrate the potential of diagnostic-free aging studies and quick onboard health assessment.

RESULTS

Data generation

Three datasets are evaluated in this work. First, 236 cylindrical 21700 cells ($Li(Ni,Co,Al)O_2$/graphite + SiO_x) extracted from a Tesla Model 3 EV were selected from the dataset presented in van Vlijmen et al.[6] These cells were cycled under 126 distinct operating conditions, including 43 charging protocols, 14 discharging protocols, and 13 voltage windows. This extensive range of test conditions produced complex and varied degradation curves with a broad distribution of equivalent full cycles (EFCs) at the end of life. The typical procedure for battery aging is illustrated in Figure 1A. The SOH was evaluated with a diagnostic test, where the pseudo-OCV was obtained from a

Please cite this article in press as: Che et al., Diagnostic-free onboard battery health assessment, Joule (2025), https://doi.org/10.1016/j.joule.2025.102010

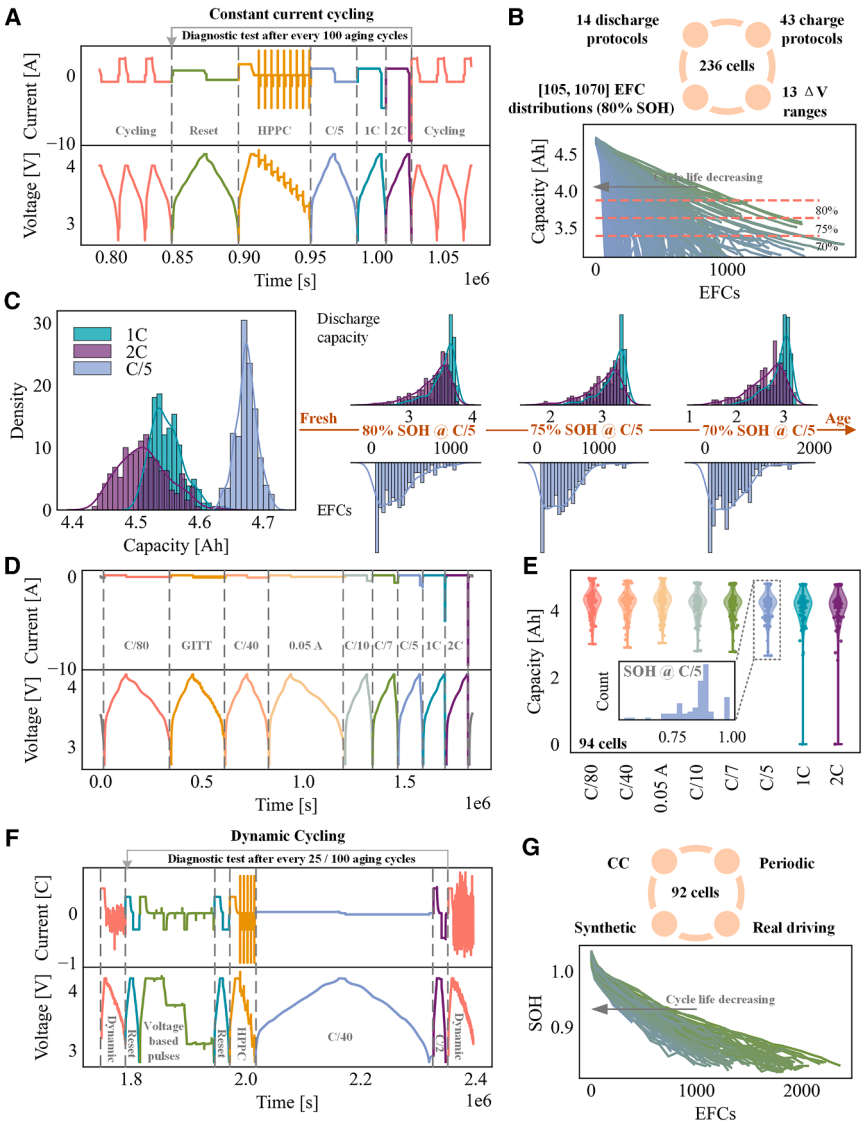

Figure 1. Data illustration

(A) Protocol for battery aging in the van Vlijmen et al. dataset, which includes the cycling and diagnostic test. The cycling test uses different C-rates and SOC windows for charging and discharging, while the pseudo-OCV curves are obtained from the diagnostic cycle.

(B) Summary of the testing conditions and the degradation curves of the test batteries.

(C) Capacity distributions obtained by different discharge C-rates and the variations during aging.[6]

(D) Protocol for the different C-rate tests generated in this work, where 8 different rate tests are included.

(E) Capacity distributions of the cells at different discharge C-rates.

(F) Protocol design for battery aging in the Geslin et al. dataset,[7] which includes the dynamic cycling and diagnostic test.

(G) Cycling design and the degradation curves for the 92 cells in the Geslin et al. dataset[7].

C/5-based reference performance test (RPT). The aging cycles consist of different charging and discharging protocols to cycle the cells within various voltage ranges for approximately 100 cycles before another diagnostic cycle is performed. Due to battery manufacturing variability and diverse aging conditions, various degradation patterns were observed, as depicted in Figure 1B and details described in van Vlijmen et al.[6] The distribution of 1 C and 2 C at fixed C/5 SOH in Figure 1C (see Note S1, Figures S1–S3, and Table S1 for details) indicates that the mapping relationships between higher C-rates and reference RPT (C/5) are complex and diverse across different cycling conditions.

While the lowest rate used in the van Vlijmen et al. dataset is C/5, lower C-rate testing, such as C/40, is typically used for effective mechanistic feature extraction in aging analysis.[21,49–51] Obtaining these pseudo-OCV curves at different SOHs is time-consuming, yet essential to develop accurate state monitoring. To showcase the robustness of the model architecture when applied to a variety of C-rate cases for broader application interests, 94 cells from the van Vlijmen et al.[6] dataset at different SOHs were subjected to additional tests to generate a new dataset. An RPT was conducted using eight different C-rates, as shown in Figure 1D. The discharge capacities at different C-rates shown in Figure 1E illustrate the large variations in RPT and mechanistic health status among these cells. In particular, these large variations highlight the difficulty in using high C-rate data to predict and understand low-rate data. Consequently, this dataset encompasses a wide range of aging stages, from fresh cells to retired ones, enabling a holistic study of battery aging over the entire lifespan and enabling validations for health diagnostics under different C-rate tests. For more details on the data samples, see Note S2 and Figures S4 and S5.

Finally, the van Vlijmen et al. dataset and the different C-rate validation dataset use CC cycling; however, dynamic cycling is more representative of EV operations and leads to a prolonged lifetime compared with standard CC cycling.[7] Therefore, model performance in operation closer to real-world aging is crucial. To this end, we use 92 cells from the Geslin et al. dataset[7] as the third test case. The batteries were subject to four types of operating conditions, i.e., CC, periodic, synthetic, and real driving protocols. A periodic diagnostic cycle is conducted after every 25/100 aging cycles. The typical profile and the degradation curves are shown in Figures 1F and 1G. During the diagnostic test, RPT was performed under C/40, providing data closer to real OCV for the verification of our model. The diversity of degradation during practical cycling further motivates the utility of onboard health assessment during operation.

Please cite this article in press as: Che et al., Diagnostic-free onboard battery health assessment, Joule (2025), https://doi.org/10.1016/j.joule.2025.102010

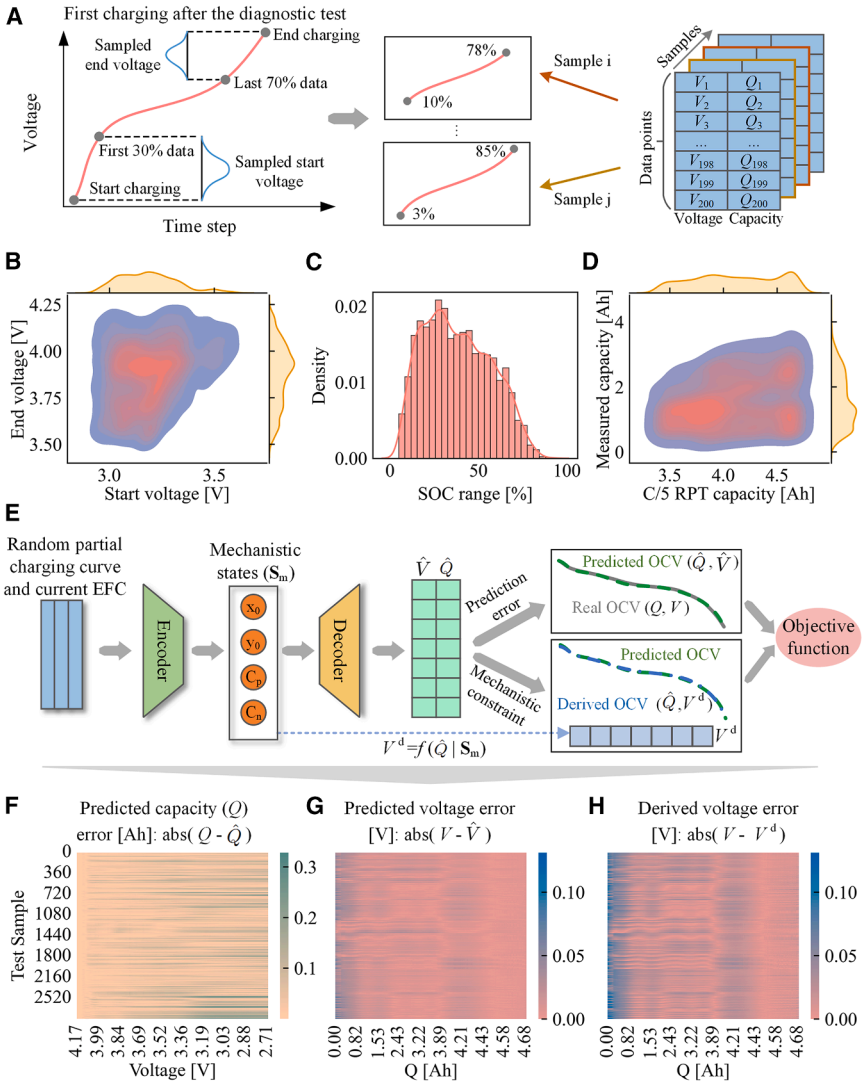

Figure 2. Data sampling and diagnostic model

(A) Randomly sampled portions of charging curves.

(B) Distributions of the voltage windows for the input data sampling of the cycling dataset.

(C) The SOC ranges of the extracted partial charging data.

(D) The mapping between the measured capacity from the partial charging and the reference C/5 RPT capacity.

(E) Mechanistic constraint model for battery health diagnosis using randomly sampled portions of charging curves.

(F and G) The errors of the $\hat{Q}$ sequence and $\hat{V}$ sequence of the predicted OCV curves for all the test samples (composed of all the RPT cycles from the test cells), respectively.

(H) The errors of the derived voltage of the OCV curves, which are calculated based on the physics-constrained mechanistic states in the machine learning model. The predicted discharge capacity ($\hat{Q}$) and voltage ($\hat{V}$) MAE errors were 45.1 mAh and 10.1 mV, respectively, with derived voltages (V^d) showing MAE error below 18.4 mV.

Health diagnosis

First, we evaluate our model on the van Vlijmen et al. dataset. The first charge (with rates between C/5 and 2C) after the diagnostic cycle is used as the input to the model, and the output is the full C/5 discharge curve of the directly preceding diagnostic cycle, which will be used as the *pseudo*-OCV curve in this study. In a real-world scenario, an EV battery may be charged between a variety of SOC ranges depending on its daily driving requirements. Although the SOC ranges and charging C-rates are already varied in the van Vlijmen et al. dataset to make the model robust to a large variety of working SOC ranges, the beginning and end of the charging data are artificially truncated as demonstrated in Figure 2A (see Note S1 for details), yielding several partial charging voltage curve samples that correspond to the same C/5 discharge curve for model training. The random sampling of the partial curves is performed three times with different starting and ending points at each diagnostic cycle to cover wide data distributions, which helps evaluate the model more comprehensively. The truncated voltage and capacity, together with current EFC, are employed as input data for the full OCV (C/5 discharge curve) predictions. Figure 2B demonstrates the distributions of the data samples with different voltage windows, and the corresponding SOC ranges are shown in Figure 2C. Based on previous studies that assessed daily usage conditions in real-world applications, where the available SOC ranges could significantly vary depending on the applications and usage habits, our data sampling effectively simulates practical charging scenarios.[2,23,52–56] The relationship between partially charged capacities from randomly sampled portions of charging processes and the reference capacity (C/5 discharge capacity) is illustrated in Figure 2D, demonstrating a significant nonlinearity.

To go from the partial charging curves to the full C/5 discharge voltage curves, the encoder-decoder structure is employed for the data-driven health diagnosis, as represented by Figure 2E. Specifically, the encoder takes the partial charging voltage, capacity, and EFC and encodes them into 4 latent variables. These latent variables are assigned to be the mechanistic states used in DVA: anode capacity (C_n), cathode capacity (C_p), anode (x_0), and cathode lithiation state (y_0) at the beginning of discharge of the corresponding half cell. These latent variables become these mechanistic states through the mechanistic constraint, which compares the derived OCV from these latent variables to the predicted OCV (see Notes S3 and S4, Figures S6 and S7, and Table S2 for detailed descriptions of the model and physics constraints). The decoder uses these mechanistic states and outputs the C/5 discharge curve. The objective function is a combination of the prediction error and the mechanistic constraint

error. In summary, this model can be understood as being first a flexible DVA where the encoder portion enables performing the analysis on partial charging data, followed by a decoder that enables flexible reconstructing of the voltage curve that balances pure DVA reconstruction (mechanistic constraint) and a component that adjusts the voltage curves to account for the discrepancy (prediction error).

To comprehensively evaluate the model, all cells with the same charging/discharging protocols appeared only in either the training or testing group. This setup ensured that the testing cells were aged under conditions unseen in the training data. Additionally, 20% of the training data were randomly chosen as validation samples to avoid overfitting by early stopping, thus establishing an inner loop for validation and an outer loop for testing (see Table S3 for the detailed grouping information). Figures 2F and 2G show the prediction results for the OCV curve, and the derived OCV (representing the OCV curve obtained directly by the constrained mechanistic states) is shown in Figure 2H. The heat maps reflect the capacity/voltage error at each voltage/capacity point for all the test OCV curves, where the color bars represent the absolute errors. The results indicate the stability of the physics-constrained machine learning model for health diagnosis across batteries operating under diverse C-rates, SOC ranges, and aging states. The mean absolute error (MAE) for the predicted discharge capacity ($\widehat{Q}$) and voltage ($\widehat{V}$) errors are 45.1 mAh (0.93% of the nominal capacity) and 10.1 mV, respectively, with derived voltages (V^{d}) with MAE of 18.4 mV, as summarized in Table 1. Due to the variations in open-circuit overpotential during aging, especially for the silicon-graphite anode, inhomogeneities of lithiation, and other aging-related influences,[20–22] we observe that while the predicted voltage error and the derived voltage error have a qualitatively similar error dependence on capacity, the predicted voltage errors (Figure 2G) are lower, indicating that the decoder can compensate for deficiencies in the mechanistic model during aging.

Here, we compare our model accuracy and complexity by incorporating different neural networks—including multilayer perceptron, recurrent neural network, gated recurrent unit neural network, long-short term memory neural network, and 1D convolutional neural network—which are widely used in battery health diagnosis and prognosis.[12,37,42,57] See Note S5 and Figure S8 for the detailed comparisons. The prediction results indicate that SOH estimation errors remained below 7% under all conditions, with more than 95% of the results having relative errors below 5% using a simple multilayer perception model as encoder and decoder. The error distributions shown in Figure S9 indicate that the estimations are not sensitive to input voltage and SOC ranges. The performance underscores the high reliability of the model for SOH estimation across diverse application scenarios.

Exemplary prediction results for the C/5 pseudo-OCV and differential voltage curves are shown in Figures 3A, 3B, and S10, demonstrating the effectiveness and physical interpretability of the model through the comparative results with conventional offline model fitting.[17–19] The directly predicted OCV, derived OCV, and half-cell voltage facilitate the interpretation of holistic health status using only the information from the randomly sampled portions of the charging curve. The mechanistic states capture the aging, and the decoder further compensates for the prediction errors. To illustrate the role of mechanistic constraints in the data-driven model, we present the result of the ablation experiment where predictions were made without the physical constraint and the corresponding boundary constraint (L_{phy} and L_{bound} in Note S3) in Figure S11. While a pure data-driven OCV prediction model[37–40] can accurately predict OCV curves based on partial charging data to some degree, a significant misalignment between the predicted and derived OCV curves (see Figure S11A) indicates that the model functions as a black box with poor physical interpretability. Additionally, the derived OCV curve can extend beyond reasonable ranges without boundary constraints, interrupting the interpretation of aging mechanisms in a purely data-driven model. Further results from the proposed model, including the worst and average diagnosis performances across all tests, are provided in Figure S12.

With this model, we can now generate the C/5 discharge voltage curves using the charging portion of operational data without a separate diagnostic cycle. In Figure 3C, we extract the mechanistic states from an example cell using solely the aging cycle data. For the complete prediction of the C/5 discharge curves for every aging cycle of this representative cell, see Figure S13. From this analysis, we can see how the full SOC range diagnostic cycle modifies the state of the battery and generates a capacity increase that is often observed in battery degradation studies.[5,58] This approach enables a full trajectory picture of degradation in the battery that is otherwise inaccessible.

This approach is applied to all the testing cells in the dataset, and from these mechanistic states, we can directly obtain the degradation modes: LLI and LAM on the cathode (LAM_p) and anode (LAM_n). Results in Figures 3D–3F illustrate the degradation of each aging mode derived from our model, with the variations of each mechanistic state shown in Figure S14. The results indicate that the anode degradation progresses more rapidly than the cathode degradation, leading to greater losses of active material on the anode. The lithium inventory also exhibits a rapid decline, as shown in the diagnosis results. The $Li(Ni,Co,Al)O_2$/graphite + SiO_x cells used for the aging test have a strong coupling between LLI and LAM_n (Figure S15). As the anode is a blended graphite SiO_x electrode, swelling of Si with Li intercalation can cause cracking of particles and disconnection, creating "dead" particles with trapped/lost Li.[59–61] LAM_p is also correlated with LLI, as demonstrated in Figure S15. Possible causes are oxidation-induced cation disordering or cathode-electrolyte interphase (CEI) growth, degrading the cathode while trapping dead Li in blocked crystal sites.[59,61,62]

Shapley additive explanations (SHAP), a tool for analyzing the importance of input features on the output, is used in combination with our model to further interpret our results.[6,7,63–66] The SHAP analysis for the encoder is presented in Figure 3G, while the results for the decoder are illustrated in Figure 3H. For most of the mechanistic states, voltage, capacity, and EFC are approximately equal in determining the output. For the decoder, however, the anode capacity contributes most significantly to the reconstruction of the voltage curve. The aging mode analysis indicates a more pronounced degradation of LAM_n compared

Table 1. Summary of the diagnostic and prognostic performances

Objective	Task	RMSE	MAE	R^2
Health diagnosis (dataset 1)	predicted Q of OCV curve ($\widehat{Q}$)	67.2 mAh	45.1 mAh	0.998
	predicted voltage of OCV curve ($\widehat{V}$)	13.8 mV	10.1 mV	0.999
	derived voltage of OCV curve (V^d)	25.2 mV	18.4 mV	0.996
	predicted SOH	1.86%	1.35%	0.945
Health prognosis (dataset 1)	predicted Q of the future degradation curve	28.7 mAh	22.6 mAh	0.861
	predicted EFC of future degradation curve	62.1 EFC	39.4 EFC	0.910
	predicted cycle life from degradation curve	105 EFC	76.0 EFC	0.824
	predicted cycle life from model	105 EFC	76.4 EFC	0.824
	predicted cycle life for all cells	81.6 EFC	59.2 EFC	0.876
Early health prognosis (dataset 1)	predicted Q of the future degradation curve	70.2 mAh	50.0 mAh	0.842
	predicted EFC of future degradation curve	93.6 EFC	60.1 EFC	0.636
	predicted cycle life from degradation curve	158 EFC	118 EFC	0.482
	predicted cycle life from model	158 EFC	118 EFC	0.481
	predicted cycle life for all cells	95.9 EFC	65.1 EFC	0.794
Different C-rate validations (dataset 2)	predicted Q of OCV curve ($\widehat{Q}$)	68.2 mAh	43.1 mAh	0.997
	predicted voltage of OCV curve ($\widehat{V}$)	27.4 mV	22.4 mV	0.996
	derived voltage of OCV curve (V^d)	52.4 mV	43.1 mV	0.984
	predicted SOH	2.54%	1.86%	0.890
Dynamic cycling using charging (dataset 3)	predicted Q of OCV curve ($\widehat{Q}$)	0.61%	0.41%	0.999
	predicted voltage of OCV curve ($\widehat{V}$)	4.79 mV	5.05 mV	0.999
	derived voltage of OCV curve (V^d)	11.4 mV	8.46 mV	0.999
	predicted SOH	1.10%	0.86%	0.963
Dynamic cycling using discharging (dataset 3)	predicted Q of OCV curve ($\widehat{Q}$)	0.79%	0.53%	0.999
	predicted voltage of OCV curve ($\widehat{V}$)	9.63 mV	7.33 mV	0.999
	derived voltage of OCV curve (V^d)	18.1 mV	13.7 mV	0.999
	predicted SOH	1.51%	1.15%	0.932

Note: datasets 1, 2, and 3 in the table correspond to the van Vlijmen et al. dataset (CC cycling), the different C-rates dataset (RPT using different C-rates), and the Geslin et al. dataset (dynamic cycling), respectively.

with LAM_p, which is corroborated by the SHAP results. In addition, due to the fact that the anode is a blended electrode, the decoder may need to compensate for the voltage effects of preferential degradation of Si.[21,67] The analysis highlights that capacity degradation on the anode has a greater impact on health predictions than capacity degradation on the cathode, as depicted in Figure 3H. Additional results detailing the impact of features on mechanistic state estimations can be found in Figure S16. In summary, with the proposed diagnostic-free physics-constrained health diagnosis model, the degradation mechanisms and pathways can be reconstructed in regular usage by only using the partial charging measurements across various SOC ranges and C-rates for the whole lifespan.

Health prognosis

In addition to health diagnosis to understand current aging conditions, health prognosis is essential to anticipate future degradation to guide predictive maintenance and reduce research and development costs. Future degradation can be forecasted using the macroscopic (current EFC and predicted SOH at the current cycle, i.e., the last value of $\widehat{Q}$ sequence) and mechanistic states (C_p, C_n, x_0, and y_0) through another decoder, as shown in Figure S6. The data-driven diagnostic results are utilized as the basis for future degradation prediction, without needing access to historical degradation data. This allows for developing a sequential framework for health diagnosis and prognosis (as detailed in Note S3). Such a framework facilitates real-world applications by eliminating the need for increased memory capacity in the battery management system for health prognosis, which conventional degradation prediction models typically require.

The predicted results for the cycle life and future degradation curves are shown in Figures 4A–4C, where the predictions of cycle life (when the capacity C/5 RPT drops below 80% of the nominal capacity) and future degradation curves are demonstrated. The predictions here show the results when the diagnostic cycle is conducted between 83.5% and 86.5% SOH (for an application of guiding onboard predictive maintenance), with earlier prediction results from the third diagnostic cycle presented in Figure S17 (for an application of early prediction). The results indicate that the prediction successfully converges to real degradation and predicts the cycle life with mean errors of less than 76 EFCs, 12.8% of the mean cycle life of 593 EFCs. The predicted cycle life (represented by the EFC) can be determined either from the final value of the future degradation curve (sequence prediction) or directly from the decoder (point prediction), with

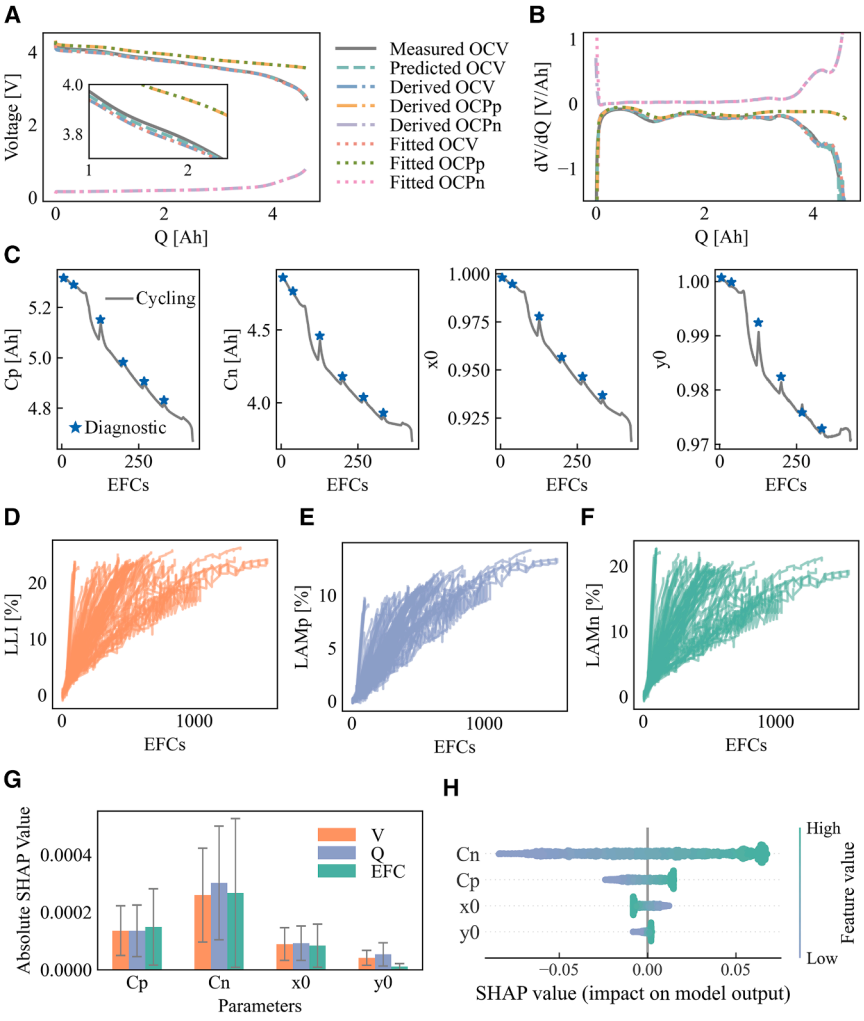

Figure 3. Health diagnosis

(A) Illustration of the predicted OCV curves, derived OCV curves based on the constrained mechanistic states, and the fitted OCV based on the states obtained by the particle swarm optimization for the predicted OCV curves.

(B) The differential voltage curves for the corresponding curves in (A).

(C) The predicted curves of the mechanistic states obtained from cycling cycles and the comparisons from those obtained from diagnostic cycles.

(D–F) The predicted aging modes, which are directly obtained based on the constrained mechanistic states, for onboard diagnosis of LLI, LAM at the cathode (LAM_p), and LAM at the anode (LAM_n).

(G) The SHAP analysis results for the encoder, which represents the impacts (absolute values) of the input information from the partial charging curve on the prediction of mechanistic states.

(H) The SHAP analysis of the decoder for the OCV curve predictions, where the impacts of the constrained mechanistic states on the predicted OCV (combination impacts of the capacity and voltage) are illustrated.

the comparable performance shown in Table 1. The mean prediction error for early predictions (i.e., predictions from the third diagnostic cycle) is also less than 118 EFCs, and the future capacity degradation curve shows an MAE and root-mean-square error (RMSE) of less than 50.1 and 70.1 mAh, respectively, for these cells having a nominal capacity of 4.84 Ah. Therefore, the model enables health prognosis for both future degradation curves and cycle life using only onboard measurements, without requiring historical memory. Improved prediction accuracy throughout the aging process supports better predictive maintenance and retirement planning.

To evaluate the feature impacts of the health prognosis decoder, SHAP analysis results are shown in Figures 4D–4H. Each row of the heatmap in Figures 4D and 4E represents the mechanistic and macroscopic features influencing the predicted future degradation curves, described by the variation in capacities and EFCs. The mean impacts on the future degradation curves for the EFCs and capacities are shown in Figures 4F and 4H, where the current EFC has the highest importance. The anode state has a greater influence on future EFC predictions, while the cathode has a more significant impact on future capacity predictions. The final prediction step of the future EFCs, which represents the cycle life prediction, is analyzed in Figure 4G, highlighting the substantial impacts of both mechanistic and macroscopic features on the predictions. The SHAP results for the prediction of cycle life point, as shown in Figure S18, reveal a similar impact of features on the outcomes. When predictions are made at an earlier stage, such as during the third diagnostic cycle as illustrated in Figure S17, the feature impacts on future degradation and cycle life predictions exhibit some differences, with mechanistic features playing more prominent roles, especially for the capacity from the anode. This result successfully captures the main aging effects in early life. One physical reason for the differences in the features' impacts is that the overpotential of half cells may change during aging, leading to a decreasing effect on the mechanistic states extracted in later aging status. In conclusion, the physically constrained health diagnosis model effectively extracts mechanistic states onboard, facilitating a better early health prognosis and cycle life predictions, which help guide better maintenance and retirement.

Applications to diverse use conditions

In the van Vlijmen et al. dataset, C/5 discharge data were used as the target pseudo-OCV; however, this is a higher rate than what is typically used in DVA. To address this issue, 94 cells at a variety of SOH (Figure 5A), calculated by C/5 capacity, were sampled from the van Vlijmen et al. dataset and underwent testing under eight different C-rates with rates as low as C/80 (Figure 5D). Here we deploy the model pre-trained on the van

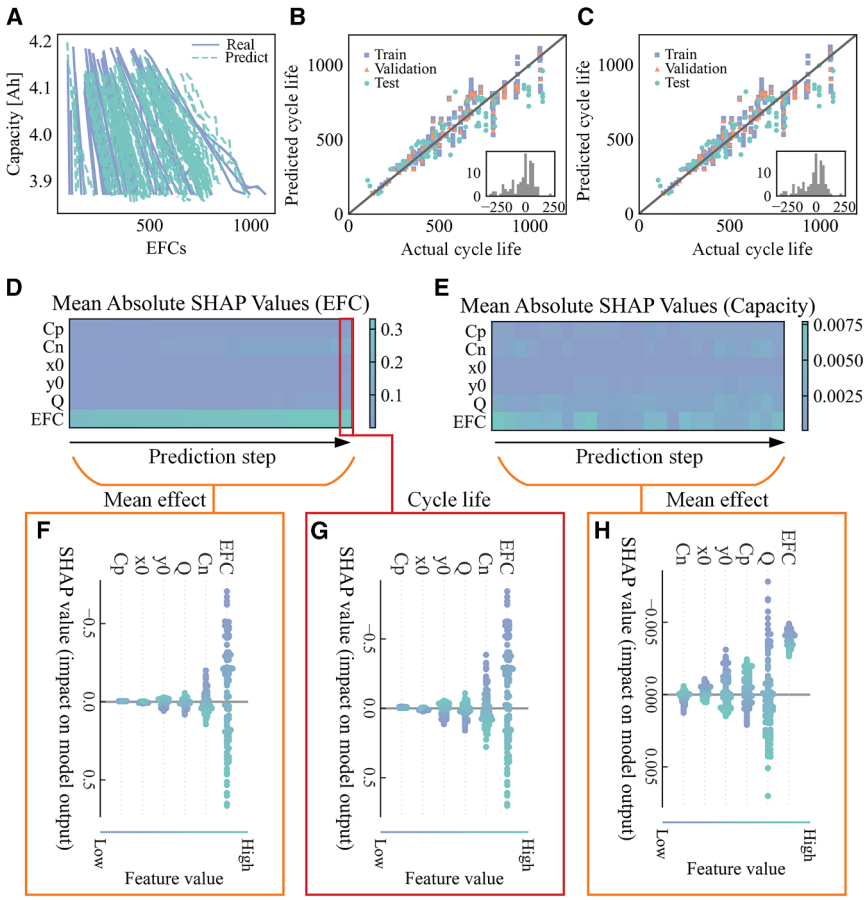

Figure 4. Future health prognosis

(A) Prediction of future capacity degradation curves.

(B) Sequence prediction of the cycle life from the last value of the predicted future degradation curve.

(C) Point prediction of the cycle life based on the decoder.

(D and E) The feature impacts analysis of the future degradation predictions based on SHAP for the predicted EFC and capacity values, respectively. The color bars indicate the SHAP values.

(F) The mean feature impacts the predicted future EFC variations.

(G) The feature impacts on the last prediction step, i.e., the cycle life, of the predicted EFCs.

(H) The mean feature impacts the predicted capacities.

Vlijmen et al. dataset and fine-tune it to use the partial discharge data from 20 min of a 1 C discharge as the input to predict the voltage curve and capacity at different C-rates (Figure 5B). Detailed explanations are provided in Notes S2 and S3. The effectiveness of our model for different C-rate validations is illustrated in Figure 5C, where 5-fold cross-validation was performed, and results for all cells are displayed. Performance of the C/80 pseudo-OCV curve and differential voltage curve predictions for four example cells at different SOH are shown in Figures 5D and 5E (SOH based on C/80 capacity). This model demonstrates significant time savings, effectively extracting the low C-rate voltage curves using only 20 min of 1 C discharge data compared with the nearly 80 h needed to gather a C/80 pseudo-OCV curve. The cells are under varying SOH conditions, and our model enables fast health assessment to guide intelligent and fast sorting, regrouping, and reusing of these batteries, which is significant for second-life applications.

Additional results on prediction performance and DVA are provided in Figures S19 and S20. Figure S21 summarizes the prediction outcomes, indicating high accuracy and reliability, with an MAE for predicted capacity and voltage of less than 43.2 mAh and 22.4 mV, respectively, and R^2 values exceeding 0.99. Even with a shorter partial discharge, our model maintains strong performance. See Figures S22 and S23 for results from the 10-min discharge-based assessment, demonstrating the model's effectiveness with reduced test times. See Figure S24 for the impact interpretations based on SHAP analysis, where the results also indicate the pronounced impact of anode degradations. In addition, the correlations of the predicted results from C/5 and C/40 are demonstrated in Figure S25. By applying a quick and flexible fine-tuning strategy to the model developed for onboard health diagnosis, our model transitions seamlessly to predicting different C-rate behaviors. RPT capacities at different low C-rates can be predicted from partial discharge curves at 1 C, and the mechanistic states that are directly obtained through this process are shown in Figure 5F. Therefore, our model is suitable for applications in the fast retirement assessment with physical interpretations.

In real-world applications, although CC or power may be seen during charging, it is rarely seen during operation or discharge. While the batteries in the Geslin et al. dataset are charged identically, they are discharged under several different dynamic discharge loading profiles. We apply our model to the Geslin et al. dataset[7] to validate our model performance under real-world operating conditions. Before using the dynamic discharge data as an input, we first use the charging data as a baseline. The same data sampling technique employed for the van Vlijmen et al. dataset is utilized here, where randomly sampled portions of charging curves are extracted from the charging data following the diagnostic cycle for model input, while the C/40 discharge pseudo-OCV serves as the output. The model pretrained by the Vlijmen et al. dataset is fine-tuned by using approximately one-third of the cells and subsequently tested on the remaining cells. Results are presented in Figures S26 and S27, with numerical outcomes detailed in Table 1. The prediction errors are demonstrated in Figure S28 for the predicted OCV and SOH (calculated by C/40 capacity), demonstrating high accuracy and robustness across various dynamic cycling conditions that are closer to practical operation scenarios, with

Please cite this article in press as: Che et al., Diagnostic-free onboard battery health assessment, Joule (2025), https://doi.org/10.1016/j.joule.2025.102010

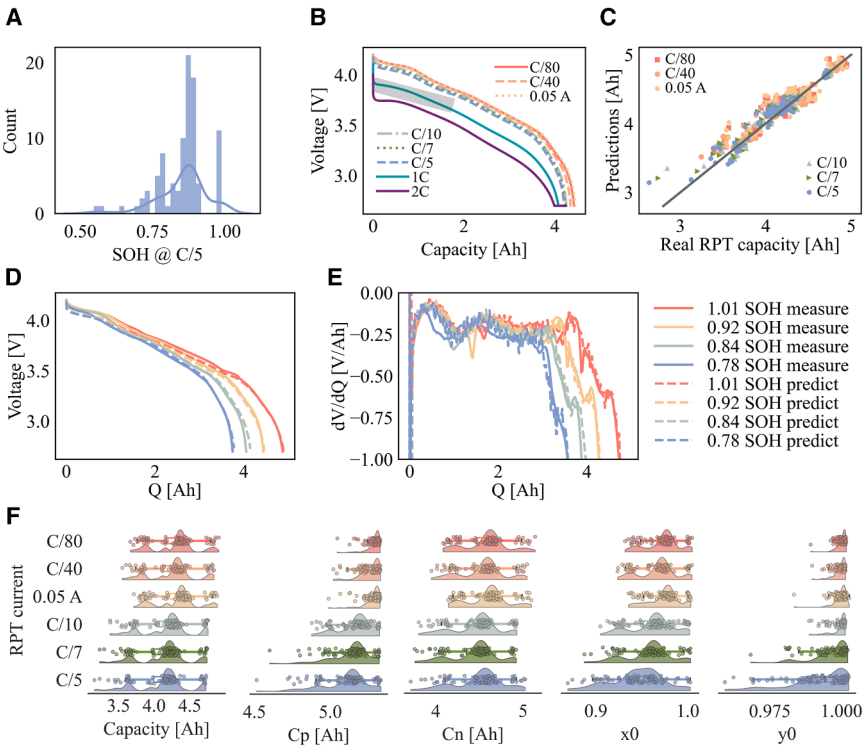

Figure 5. Rate test validation study

(A) SOH distribution (C/5 discharge) of all the cells.

(B) Discharge curves with different C-rates.

(C) Predicted capacity for different C-rate validations using measurements from 1 C discharge within 20 min.

(D) Measured OCV and predicted OCV curves using partial 1 C discharge curves under C/80 at four different SOH levels.

(E) dV/dQ curves derived from the OCV curves in (D).

(F) Prediction distributions for the discharge capacities using different C-rates and the corresponding constrained mechanistic states.

MAEs of 5.05 mV and 0.41% for the predicted voltage and normalized capacity of the OCV curves, and the SOH has an MAE of 0.86%. Even in this low C-rate OCV case, the predicted OCV has higher accuracy than the derived OCV based on the mechanistic model, again indicating that variations of the half-cell open-circuit curve and other dynamics influence the effectiveness of the mechanistic model.

Now, to see if our model can work under practical operating conditions, we instead use randomly sampled portions of the dynamic discharge curves as input for the OCV predictions. The model performance is illustrated in Figure 6, where the overall error distributions for the predicted and derived OCV are presented in Figure 6A. The results indicate good predictions with an MAE of only 7.33 mV and 0.53% for the voltage and normalized capacity of the predicted OCV curves, respectively. The distribution of the accumulated SOH prediction error is shown in Figure 6B, which indicates high prediction accuracy and reliability (95% of the results have errors less than 3.2%) under different loading profiles, C-rates, and portion data distributions (more results are shown in Figure S29). Three representative prediction results based on truncated dynamic discharge data from periodic, synthetic, and real driving discharging curves are shown in Figure 6C, indicating the effectiveness of our model with different dynamic discharging profiles. Although the results utilizing the constant current charging data create more accurate models, we show that reasonable model performance can be achieved even when using the dynamic discharge data. These findings underscore the model's potential for onboard, diagnostic test-free battery health assessment not only under CC profiles but also dynamic profiles. In summary, our model is applicable for real-world applications with EV driving cycles, where the health mechanisms and key mechanistic parameters are available to support the accurate state monitoring.

DISCUSSION

In summary, we develop an interpretable machine learning model to enable onboard battery health diagnosis and prognosis without time-consuming and disruptive diagnostic tests. We demonstrate the path for combining mechanistic constraints with machine learning, leading to a physically interpretable and robust model. The mechanistic constraints derived from DVA are integrated in the encoder-decoder framework to enable a physically interpretable latent space and thus specify the physical functions of the model. By only using the onboard measurement from CC charging or dynamic current discharging, degradation pathways can be reconstructed, and the mechanisms are available without offline diagnostic tests. To evaluate the versatility of this model, we apply our framework to three battery-cycling datasets, encompassing a total of 422 cells. First, we use the van Vlijmen et al. dataset to reconstruct C/5 diagnostic cycle data from CC cycling across various SOC windows. Results show highly accurate health diagnosis with an MAE of only 1.35% for the whole lifespan until SOH drops below 70%, while the early health prognosis achieves an EFC prediction error of less than 120. Next, we generate a new rate-performance dataset by testing rates as low as C/80 with 94 degraded cells from the van Vlijmen et al. study. Using this dataset, we fine-tune the model to reconstruct information from low-rate-performance tests (such as C/80 and C/40), leveraging partial data from a 1 C discharge, and achieve fast health diagnosis with an MAE of only 1.86% at varying SOH levels. Finally, we fine-tune the model to reconstruct C/40 diagnostic cycle data using partial dynamic operating condition data from the Geslin et al. dataset, which shows the proposed physics-constrained model is effective under real-world dynamic discharging conditions with an MAE of less than 1.2%. Therefore, once the model is trained or fine-tuned to a given system, diagnostic-free onboard battery health assessment is possible. By applying this framework across

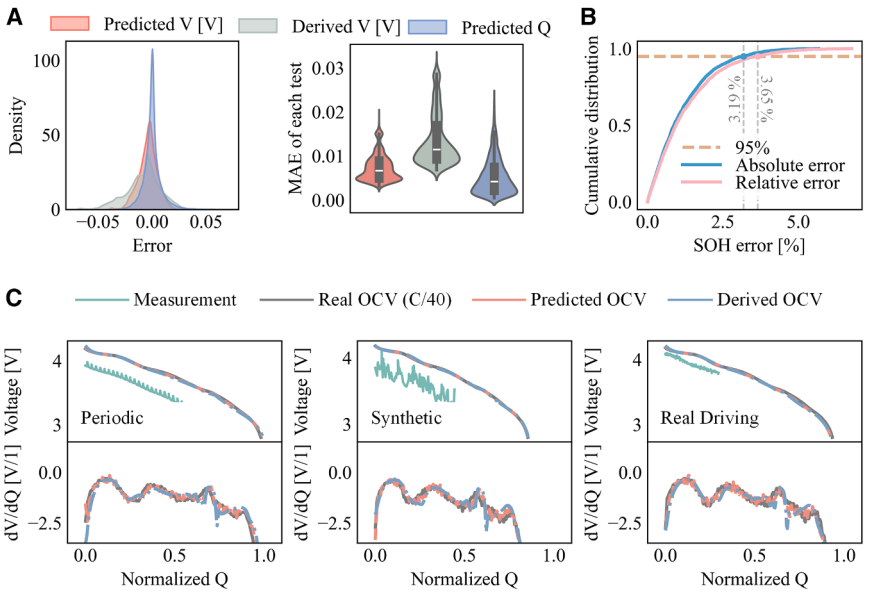

Figure 6. Validations with dynamic cycling

The partial discharging data with different loading profiles and C-rates are employed as model input to predict the OCV of the C/40 discharge.

(A) The error distributions of predicted OCV curves and derived OCV curves for the dynamic cycling dataset. The MAE of each predicted and derived OCV curve of the dynamic cycling dataset.

(B) The cumulative error distribution of the SOH estimation results.

(C) Prediction results for three representative cycling conditions, including discharging with periodic, synthetic, and real driving profiles.

these three datasets, we demonstrate its utility in enabling diagnostic-free onboard battery diagnosis and prognosis.

Our model can be flexibly applied across broad application interests such as materials and mechanisms evaluation, synthetic data generation, electric transportation health assessment, and fast retiring assessment for guiding second-life applications, with slight fine-tuning. We encourage future work in this field to further understand the detrimental effect of diagnostic cycles on battery aging with different chemistries and to utilize diagnostic-free battery health monitors to circumvent these issues.

METHODS

Experiment and data generation

236 batteries with a cathode of nickel cobalt aluminum (NCA) and an anode of graphite SiO_x from the van Vlijmen et al.[6] dataset are selected in the first dataset. The cells aged below 80%, and the available raw data are used in this work. More details of the experiment description are found in van Vlijmen et al.[6] All the data is processed through the BEEP processing pipeline.[68] These cells are cycled with different C-rates and SOC windows. A diagnostic test is performed periodically, which includes a reset cycle, hybrid pulse power characterization (HPPC), and RPT at three C-rates (C/5, 1 C, and 2 C). 94 batteries are collected for the different C-rate validation tests using the same test platform to generate the second dataset. The batteries are 21700 cylindrical cells produced by Panasonic with a nominal capacity of 4.84 Ah. These 94 cells are aged to different SOH levels through different cycling profiles. Eight different C-rates ranging from C/80 to 2 C were used for the RPT tests. Finally, the dynamic cycling dataset from Geslin et al.[7] is utilized to validate the proposed model, which is designed for real-world aging conditions. Different synthetic and real-world driving protocols with different C-rates are employed for the cycling. During the diagnostic test, voltage-based pulses are included besides reset, HPPC, and RPT tests. The RPT was performed under C/40, providing data closer to real OCV for the verification of our model. 92 commercial silicon oxide–graphite/NCA cells were cycled. For more comprehensive details, readers are referred to.[7] To obtain the anode and cathode open-circuit potential curves, we first harvested electrode sheets by disassembling the cylindrical cells used in this study within an argon glovebox. Circular sections were then punched from these electrode sheets and assembled into pouch cells with lithium metal counter electrodes. These pouch cells were subsequently cycled to extract the open-circuit potential curves of the anode and cathode for use in DVA. For further experimental details, see van Vlijmen et al.[6]

Machine learning with mechanistic constraints

Auto-encoders and decoders with physical constraints are designed for the machine learning model, where the mechanistic model describing the relationship between the four key states and the full-cell OCV is constrained to make the data-driven model interpretable. Auto-encoders and decoders can be designed as different types of neural networks, while a multilayer perceptron is simpler and easier to explain than others. In this paper, the mechanistic constraints are based on the DVA. A similar method presented in previous works is employed here.[17–19,69,70] The mechanistic model is to fit the full-cell OCV by means of two half-cell open-circuit potentials, named OCP_p for the cathode and OCP_n for the anode:

$$OCV(z) = OCP_p(y) - OCP_n(x), \qquad \text{(Equation 1)}$$

During battery aging, the variations of the full-cell OCV curve can be reconstructed through the shift and shrinking of the OCP curves. The shift and shrinking can be described by four key mechanistic states $\theta = [x_0, y_0, C_p, C_n]$, as detailed in Note S4. In this way, the non-destructive aging mode diagnosis can be performed, and the LLI and LAM at two electrodes can be obtained. Traditional methods employed model fitting to obtain these mechanistic states through diagnostic tests. In this work, instead of using offline fitting, we propose an interpretable machine learning model for onboard health diagnosis and prognosis without a diagnostic test. We construct a physical constraint as a difference between the output of the decoder (i.e., predicted

OCV) and the states encoded by the encoder through the mechanistic model equations (i.e., derived OCV). In this way, we do not need the labeled data of the mechanistic states, which are necessary for conventional supervised machine learning-based state estimation. In addition, the prior knowledge of the boundary condition (e.g., the ranges of the SOC and mechanistic states) for the prediction and constrained states helps maintain the predictions within reasonable ranges and accelerates the model convergence. Therefore, the total loss function for the health diagnosis can be described by

$$L_1 = \alpha L_{\text{reg}} + \beta L_{\text{phy}} + \sum_{i=1}^{N} \gamma_i L_{\text{bound},i}, \quad \text{(Equation 2)}$$

where L_{reg}, L_{phy}, and L_{bound} represent the loss for the prediction, physical constraints, and boundary constraints, respectively, and α, β, and γ are the associated weighting factors. For prognosis, the regression loss and boundary knowledge are included for the prognosis decoder training, and the total loss is

$$L_2 = \eta L_{\text{reg}} + \sum_{i=1}^{N} \zeta_i L_{\text{bound},i}, \quad \text{(Equation 3)}$$

where η and ζ are also the weighting factors. The model is developed through PyTorch. The weights of the regression loss and physical loss were set equal to the same value (1.0) so that the model prediction accuracy and mechanistic modeling equations have the same importance. For the boundary loss, we constrained ten boundaries, so the weight for each boundary was set to 0.1 so that the sum over the ten boundaries is weighed the same as the regression loss and physical loss. To understand the feature impacts on the diagnosis and prognosis performance, we use the SHAP Python library for the encoder and decoder, respectively. See Notes S3 and S6 for detailed descriptions of the machine learning model and SHAP analysis.[63,64]

RESOURCE AVAILABILITY

Lead contact

Requests for further information and resources should be directed to and will be fulfilled by the lead contact, Richard D. Braatz (braatz@mit.edu).

Materials availability

This study did not generate new materials.

Data and code availability

Data and code are available at https://data.matr.io/10/.

ACKNOWLEDGMENTS

This work was supported by the Toyota Research Institute through the Accelerated Materials Design and Discovery program. Y.C. acknowledges support from the Independent Research Foundation Denmark and the Novo Nordisk Foundation. The authors would like to thank A. Geslin and X. Cui for their thoughtful comments and feedback on the paper.

AUTHOR CONTRIBUTIONS

Conceptualization, Y.C. and R.D.B.; methodology, Y.C., V.N.L., J.R., J.S., and R.D.B.; investigation, Y.C., V.N.L., J.R., and J.S.; writing – original draft, Y.C. and V.N.L.; writing – review and editing, J.R., J.S., M.K., M.Z.B., W.C.C., and R.D.B.; funding acquisition, M.Z.B., W.C.C., R.D.B., and Y.C.; resources, M.Z.B., W.C.C., and R.D.B.; supervision, M.Z.B., W.C.C., and R.D.B.

DECLARATION OF INTERESTS

The authors declare no competing interests.

SUPPLEMENTAL INFORMATION

Supplemental information can be found online at https://doi.org/10.1016/j.joule.2025.102010.

Received: March 16, 2025
Revised: May 11, 2025
Accepted: June 6, 2025

REFERENCES

1. Dunn, B., Kamath, H., and Tarascon, J.M. (2011). Electrical energy storage for the grid: A battery of choices. Science *334*, 928–935. https://doi.org/10.1126/science.1212741.
2. Schaeffer, J., Lenz, E., Gulla, D., Bazant, M.Z., Braatz, R.D., and Findeisen, R. (2024). Gaussian process-based online health monitoring and fault analysis of lithium-ion battery systems from field data. Cell Rep. Phys. Sci. *5*, 102258. https://doi.org/10.1016/j.xcrp.2024.102258.
3. Dubarry, M., Baure, G., and Devie, A. (2018). Durability and reliability of ev batteries under electric utility grid operations: Path dependence of battery degradation. J. Electrochem. Soc. *165*, A773–A783. https://doi.org/10.1149/2.0421805jes.
4. Edge, J.S., O'Kane, S., Prosser, R., Kirkaldy, N.D., Patel, A.N., Hales, A., Ghosh, A., Ai, W., Chen, J., Yang, J., et al. (2021). Lithium ion battery degradation: What you need to know. Phys. Chem. Chem. Phys. *23*, 8200–8221. https://doi.org/10.1039/D1CP00359C.
5. Lewerenz, M., Dechent, P., and Sauer, D.U. (2019). Investigation of capacity recovery during rest period at different states-of-charge after cycle life test for prismatic Li($Ni_{1/3}Mn_{1/3}Co_{1/3}$)O_2-graphite cells. J. Energy Storage *21*, 680–690. https://doi.org/10.1016/j.est.2019.01.004.
6. van Vlijmen, B., Lam, V., Asinger, P.A., Cui, X., Ganapathi, D., Sun, S., Herring, P.K., Gopal, C.B., Geise, N., Deng, H.D., et al. (2023). Interpretable data-driven modeling reveals complexity of battery aging. Preprint at ChemRxiv. https://doi.org/10.26434/chemrxiv-2023-zdl2n.
7. Geslin, A., Xu, L., Ganapathi, D., Moy, K., Chueh, W.C., and Onori, S. (2024). Dynamic cycling enhances battery lifetime. Nat. Energy *10*, 172–180. https://doi.org/10.1038/s41560-024-01675-8.
8. Zhuang, D., Li, M.L., Lam, V.N., Braatz, R.D., Chueh, W.C., and Bazant, M. Z. (2024). Physics-informed design of hybrid pulse power characterization tests for rechargeable batteries. J. Electrochem. Soc. *171*, 050510. https://doi.org/10.1149/1945-7111/ad4394.
9. Rhyu, J., Zhuang, D., Bazant, M.Z., and Braatz, R.D. (2024). Optimum model-based design of diagnostics experiments (DOE) with hybrid pulse power characterization (HPPC) for lithium-ion batteries. J. Electrochem. Soc. *171*, 070544. https://doi.org/10.1149/1945-7111/ad63ce.
10. Wang, S., Zhang, S., Wen, S., and Fernandez, C. (2024). An accurate state-of-charge estimation of lithium-ion batteries based on improved particle swarm optimization-adaptive square root cubature kalman filter. J. Power Sources *624*, 235594. https://doi.org/10.1016/j.jpowsour.2024.235594.
11. Wang, S., Wang, C., Takyi-Aninakwa, P., Jin, S., Fernandez, C., and Huang, Q. (2024). An improved parameter identification and radial basis correction-differential support vector machine strategies for state-of-charge estimation of urban-transportation-electric-vehicle lithium-ion batteries. J. Energy Storage *80*, 110222. https://doi.org/10.1016/j.est.2023.110222.

12. Tao, S., Liu, H., Sun, C., Ji, H., Ji, G., Han, Z., Gao, R., Ma, J., Ma, R., Chen, Y., et al. (2023). Collaborative and privacy-preserving retired battery sorting for profitable direct recycling via federated machine learning. Nat. Commun. *14*, 8032. https://doi.org/10.1038/s41467-023-43883-y.

13. Tao, S., Ma, R., Chen, Y., Liang, Z., Ji, H., Han, Z., Wei, G., Zhang, X., and Zhou, G. (2024). Rapid and sustainable battery health diagnosis for recycling pretreatment using fast pulse test and random forest machine learning. J. Power Sources *597*, 234156. https://doi.org/10.1016/j.jpowsour.2024.234156.

14. Mohtat, P., Lee, S., Siegel, J.B., and Stefanopoulou, A.G. (2019). Towards better estimability of electrode-specific state of health: Decoding the cell expansion. J. Power Sources *427*, 101–111. https://doi.org/10.1016/j.jpowsour.2019.03.104.

15. Dey, S., Shi, Y., Smith, K., Colclasure, A.M., and Li, X. (2020). From battery cell to electrodes: Real-time estimation of charge and health of individual battery electrodes. IEEE Trans. Ind. Electron. *67*, 2167–2175. https://doi.org/10.1109/TIE.2019.2907514.

16. Che, Y., Hu, X., and Teodorescu, R. (2023). Opportunities for battery aging mode diagnosis of renewable energy storage. Joule *7*, 1405–1407. https://doi.org/10.1016/j.joule.2023.06.014.

17. Marongiu, A., Nlandi, N., Rong, Y., and Sauer, D.U. (2016). On-board capacity estimation of lithium iron phosphate batteries by means of half-cell curves. J. Power Sources *324*, 158–169. https://doi.org/10.1016/j.jpowsour.2016.05.041.

18. Dubarry, M., Truchot, C., and Liaw, B.Y. (2012). Synthesize battery degradation modes via a diagnostic and prognostic model. J. Power Sources *219*, 204–216. https://doi.org/10.1016/j.jpowsour.2012.07.016.

19. Stadler, J., Fath, J., Ecker, M., and Latz, A. (2024). Combining a data driven and mechanistic model to predict capacity and potential curve-degradation. Batteries & Supercaps *7*, e202400211. https://doi.org/10.1002/batt.202400211.

20. Fath, J.P., Dragicevic, D., Bittel, L., Nuhic, A., Sieg, J., Hahn, S., Alsheimer, L., Spier, B., and Wetzel, T. (2019). Quantification of aging mechanisms and inhomogeneity in cycled lithium-ion cells by differential voltage analysis. J. Energy Storage *25*, 100813. https://doi.org/10.1016/j.est.2019.100813.

21. Schmitt, J., Schindler, M., Oberbauer, A., and Jossen, A. (2022). Determination of degradation modes of lithium-ion batteries considering aging-induced changes in the half-cell open-circuit potential curve of silicon–graphite. J. Power Sources *532*, 231296. https://doi.org/10.1016/j.jpowsour.2022.231296.

22. Sieg, J., Storch, M., Fath, J., Nuhic, A., Bandlow, J., Spier, B., and Sauer, D.U. (2020). Local degradation and differential voltage analysis of aged lithium-ion pouch cells. J. Energy Storage *30*, 101582. https://doi.org/10.1016/j.est.2020.101582.

23. Pozzato, G., Allam, A., Pulvirenti, L., Negoita, G.A., Paxton, W.A., and Onori, S. (2023). Analysis and key findings from real-world electric vehicle field data. Joule *7*, 2035–2053. https://doi.org/10.1016/j.joule.2023.07.018.

24. Sulzer, V., Mohtat, P., Aitio, A., Lee, S., Yeh, Y.T., Steinbacher, F., Khan, M.U., Lee, J.W., Siegel, J.B., Stefanopoulou, A.G., and Howey, D.A. (2021). The challenge and opportunity of battery lifetime prediction from field data. Joule *5*, 1934–1955. https://doi.org/10.1016/j.joule.2021.06.005.

25. Zhang, Z., Gu, X., Zhu, Y., Wang, T., Gong, Y., and Shang, Y. (2025). Data-driven available capacity estimation of lithium-ion batteries based on fragmented charge capacity. Commun. Eng. *4*, 32. https://doi.org/10.1038/s44172-025-00372-y.

26. Harper, G., Sommerville, R., Kendrick, E., Driscoll, L., Slater, P., Stolkin, R., Walton, A., Christensen, P., Heidrich, O., Lambert, S., et al. (2019). Recycling lithium-ion batteries from electric vehicles. Nature *575*, 75–86. https://doi.org/10.1038/s41586-019-1682-5.

27. Ciez, R.E., and Whitacre, J.F. (2019). Examining different recycling processes for lithium-ion batteries. Nat. Sustain. *2*, 148–156. https://doi.org/10.1038/s41893-019-0222-5.

28. Xu, P., Dai, Q., Gao, H., Liu, H., Zhang, M., Li, M., Chen, Y., An, K., Meng, Y.S., Liu, P., et al. (2020). Efficient direct recycling of lithium-ion battery cathodes by targeted healing. Joule *4*, 2609–2626. https://doi.org/10.1016/j.joule.2020.10.008.

29. Tao, S., Sun, C., Fu, S., Wang, Y., Ma, R., Han, Z., Sun, Y., Li, Y., Wei, G., Zhang, X., et al. (2023). Battery cross-operation-condition lifetime prediction via interpretable feature engineering assisted adaptive machine learning. ACS Energy Lett. *8*, 3269–3279. https://doi.org/10.1021/acsenergylett.3c01012.

30. Tao, S., Zhang, M., Zhao, Z., Li, H., Ma, R., Che, Y., Sun, X., Su, L., Sun, C., Chen, X., et al. (2025). Non-destructive degradation pattern decoupling for early battery trajectory prediction via physics-informed learning. Energy Environ. Sci. *18*, 1544–1559. https://doi.org/10.1039/D4EE03839H.

31. Roman, D., Saxena, S., Robu, V., Pecht, M., and Flynn, D. (2021). Machine learning pipeline for battery state-of-health estimation. Nat. Mach. Intell. *3*, 447–456. https://doi.org/10.1038/s42256-021-00312-3.

32. Thelen, A., Huan, X., Paulson, N., Onori, S., Hu, Z., and Hu, C. (2024). Probabilistic machine learning for battery health diagnostics and prognostics—Review and perspectives. npj Mater. Sustain. *2*, 14. https://doi.org/10.1038/s44296-024-00011-1.

33. Severson, K.A., Attia, P.M., Jin, N., Perkins, N., Jiang, B., Yang, Z., Chen, M.H., Aykol, M., Herring, P.K., Fraggedakis, D., et al. (2019). Data-driven prediction of battery cycle life before capacity degradation. Nat. Energy *4*, 383–391. https://doi.org/10.1038/s41560-019-0356-8.

34. Nozarijouybari, Z., and Fathy, H.K. (2024). Machine learning for battery systems applications: Progress, challenges, and opportunities. J. Power Sources *601*, 234272. https://doi.org/10.1016/j.jpowsour.2024.234272.

35. Hu, X., Xu, L., Lin, X., and Pecht, M. (2020). Battery lifetime prognostics. Joule *4*, 310–346. https://doi.org/10.1016/j.joule.2019.11.018.

36. Tang, X., Wang, Y., Liu, Q., and Gao, F. (2021). Reconstruction of the incremental capacity trajectories from current-varying profiles for lithium-ion batteries. iScience *24*, 103103. https://doi.org/10.1016/j.isci.2021.103103.

37. Tian, J., Xiong, R., Shen, W., and Sun, F. (2021). Electrode ageing estimation and open circuit voltage reconstruction for lithium ion batteries. Energy Storage Mater. *37*, 283–295. https://doi.org/10.1016/j.ensm.2021.02.018.

38. Hofmann, T., Hamar, J., Mager, B., Erhard, S., and Schmidt, J.P. (2024). Transfer learning from synthetic data for open-circuit voltage curve reconstruction and state of health estimation of lithium-ion batteries from partial charging segments. Energy AI *17*, 100382. https://doi.org/10.1016/j.egyai.2024.100382.

39. Su, L., Zhang, S., McGaughey, A.J.H., Reeja-Jayan, B., and Manthiram, A. (2023). Battery charge curve prediction via feature extraction and supervised machine learning. Adv. Sci. (Weinh) *10*, e2301737. https://doi.org/10.1002/advs.202301737.

40. Ko, C.J., and Chen, K.C. (2024). Using tens of seconds of relaxation voltage to estimate open circuit voltage and state of health of lithium ion batteries. Appl. Energy *357*, 122488. https://doi.org/10.1016/j.apenergy.2023.122488.

41. Aykol, M., Gopal, C.B., Anapolsky, A., Herring, P.K., van Vlijmen, B., Berliner, M.D., Bazant, M.Z., Braatz, R.D., Chueh, W.C., and Storey, B.D. (2021). Perspective—combining physics and machine learning to predict battery lifetime. J. Electrochem. Soc. *168*, 030525. https://doi.org/10.1149/1945-7111/abec55.

42. Navidi, S., Thelen, A., Li, T., and Hu, C. (2024). Physics-informed machine learning for battery degradation diagnostics: A comparison of state-of-the-art methods. Energy Storage Mater. *68*, 103343. https://doi.org/10.1016/j.ensm.2024.103343.

43. Weng, A., Mohtat, P., Attia, P.M., Sulzer, V., Lee, S., Less, G., and Stefanopoulou, A. (2021). Predicting the impact of formation protocols on battery lifetime immediately after manufacturing. Joule *5*, 2971–2992. https://doi.org/10.1016/j.joule.2021.09.015.

44. Tu, H., Moura, S., Wang, Y., and Fang, H. (2023). Integrating physics-based modeling with machine learning for lithium-ion batteries. Appl. Energy *329*, 120289. https://doi.org/10.1016/j.apenergy.2022.120289.

45. Karniadakis, G.E., Kevrekidis, I.G., Lu, L., Perdikaris, P., Wang, S., and Yang, L. (2021). Physics-informed machine learning. Nat. Rev. Phys. *3*, 422–440. https://doi.org/10.1038/s42254-021-00314-5.

46. Borah, M., Wang, Q., Moura, S., Sauer, D.U., and Li, W. (2024). Synergizing physics and machine learning for advanced battery management. Commun. Eng. *3*, 134. https://doi.org/10.1038/s44172-024-00273-6.

47. Huang, Y., Zou, C., Li, Y., and Wik, T. (2024). Minn: Learning the dynamics of differential-algebraic equations and application to battery modeling. IEEE Trans. Pattern Anal. Mach. Intell. *46*, 11331–11344. https://doi.org/10.1109/TPAMI.2024.3456475.

48. Wang, F., Zhai, Z., Zhao, Z., Di, Y., and Chen, X. (2024). Physics-informed neural network for lithium-ion battery degradation stable modeling and prognosis. Nat. Commun. *15*, 4332. https://doi.org/10.1038/s41467-024-48779-z.

49. Harlow, J.E., Ma, X., Li, J., Logan, E., Liu, Y., Zhang, N., Ma, L., Glazier, S. L., Cormier, M.M.E., Genovese, M., et al. (2019). A wide range of testing results on an excellent lithium-ion cell chemistry to be used as benchmarks for new battery technologies. J. Electrochem. Soc. *166*, A3031–A3044. https://doi.org/10.1149/2.0981913jes.

50. Dubarry, M., and Liaw, B.Y. (2009). Identify capacity fading mechanism in a commercial $LiFePO_4$ cell. J. Power Sources *194*, 541–549. https://doi.org/10.1016/j.jpowsour.2009.05.036.

51. Fly, A., and Chen, R. (2020). Rate dependency of incremental capacity analysis (dQ/dV) as a diagnostic tool for lithium-ion batteries. J. Energy Storage *29*, 101329. https://doi.org/10.1016/j.est.2020.101329.

52. Zhao, Y., Wang, Z., Shen, Z.M., and Sun, F. (2021). Assessment of battery utilization and energy consumption in the large-scale development of urban electric vehicles. Proc. Natl. Acad. Sci. USA. *118*, e2017318118. https://doi.org/10.1073/pnas.2017318118.

53. Figgener, J., van Ouwerkerk, J., Haberschusz, D., Bors, J., Woerner, P., Mennekes, M., Hildenbrand, F., Hecht, C., Kairies, K.P., Wessels, O., et al. (2024). Multi-year field measurements of home storage systems and their use in capacity estimation. Nat. Energy *9*, 1438–1447. https://doi.org/10.1038/s41560-024-01620-9.

54. Cui, D., Wang, Z., Liu, P., Wang, S., Zhang, Z., Dorrell, D.G., and Li, X. (2022). Battery electric vehicle usage pattern analysis driven by massive real-world data. Energy *250*, 123837. https://doi.org/10.1016/j.energy.2022.123837.

55. Zhao, P., Zhang, S., Santi, P., Cui, D., Wang, F., Liu, P., Zhang, Z., Liu, J., Wang, Z., Ratti, C., et al. (2024). Challenges and opportunities in truck electrification revealed by big operational data. Nat. Energy *9*, 1427–1437. https://doi.org/10.1038/s41560-024-01602-x.

56. Liu, H., Deng, Z., Yang, Y., Lu, C., Li, B., Liu, C., and Cheng, D. (2023). Capacity evaluation and degradation analysis of lithium-ion battery packs for on-road electric vehicles. J. Energy Storage *65*, 107270. https://doi.org/10.1016/j.est.2023.107270.

57. Wang, S., Fan, Y., Jin, S., Takyi-Aninakwa, P., and Fernandez, C. (2023). Improved anti-noise adaptive long short-term memory neural network modeling for the robust remaining useful life prediction of lithium-ion batteries. Reliab. Eng. Syst. Saf. *230*, 108920. https://doi.org/10.1016/j.ress.2022.108920.

58. Guo, J., Li, Y., Meng, J., Pedersen, K., Gurevich, L., and Stroe, D.I. (2022). Understanding the mechanism of capacity increase during early cycling of commercial nmc/graphite lithium-ion batteries. J. Energy Chem. *74*, 34–44. https://doi.org/10.1016/j.jechem.2022.07.005.

59. Mikheenkova, A., Smith, A.J., Frenander, K.B., Tesfamhret, Y., Chowdhury, N.R., Tai, C.W., Thiringer, T., Lindström, R.W., Hahlin, M., and Lacey, M.J. (2023). Ageing of high energy density automotive Li-Ion batteries: The effect of temperature and state-of-charge. J. Electrochem. Soc. *170*, 080503. https://doi.org/10.1149/1945-7111/aceb8f.

60. Liang, Q., and Bazant, M.Z. (2023). Hybrid-mpet: An open-source simulation software for hybrid electrode batteries. J. Electrochem. Soc. *170*, 093510. https://doi.org/10.1149/1945-7111/acf47f.

61. Kirkaldy, N., Samieian, M.A., Offer, G.J., Marinescu, M., and Patel, Y. (2024). Lithium-ion battery degradation: Comprehensive cycle ageing data and analysis for commercial 21700 cells. J. Power Sources *603*, 234185. https://doi.org/10.1016/j.jpowsour.2024.234185.

62. Zhuang, D., and Bazant, M.Z. (2022). Theory of layered-oxide cathode degradation in Li-ion batteries by oxidation-induced cation disorder. J. Electrochem. Soc. *169*, 100536. https://doi.org/10.1149/1945-7111/ac9a09.

63. Lundberg, S., and Lee, S.I. (2017). A unified approach to interpreting model predictions. In Advances in Neural Information Processing Systems 30, I. Guyon, U.V. Luxburg, S. Bengio, H. Wallach, R. Fergus, S. Vishwanathan, and R. Garnett, eds. (Curran Associates, Inc). https://proceedings.neurips.cc/paper_files/paper/2017/file/8a20a8621978632d76c43dfd28b67767-Paper.pdf.

64. Mangalathu, S., Hwang, S.H., and Jeon, J.S. (2020). Failure mode and effects analysis of RC members based on machine-learning-based SHapley Additive exPlanations (SHAP) approach. Eng. Struct. *219*, 110927. https://doi.org/10.1016/j.engstruct.2020.110927.

65. Cui, X., Kang, S.D., Wang, S., Rose, J.A., Lian, H., Geslin, A., Torrisi, S.B., Bazant, M.Z., Sun, S., and Chueh, W.C. (2024). Data-driven analysis of battery formation reveals the role of electrode utilization in extending cycle life. Joule *8*, 3072–3087. https://doi.org/10.1016/j.joule.2024.07.024.

66. Lee, G., Kim, J., and Lee, C. (2022). State-of-health estimation of Li-ion batteries in the early phases of qualification tests: An interpretable machine learning approach. Expert Syst. Appl. *197*, 116817. https://doi.org/10.1016/j.eswa.2022.116817.

67. Bonkile, M.P., Jiang, Y., Kirkaldy, N., Sulzer, V., Timms, R., Wang, H., Offer, G., and Wu, B. (2024). Is silicon worth it? Modelling degradation in composite silicon–graphite lithium-ion battery electrodes. J. Power Sources *606*, 234256. https://doi.org/10.1016/j.jpowsour.2024.234256.

68. Herring, P., Balaji Gopal, C., Aykol, M., Montoya, J.H., Anapolsky, A., Attia, P.M., Gent, W., Hummelshøj, J.S., Hung, L., Kwon, H.K., et al. (2020). BEEP: a python library for battery evaluation and early prediction. SoftwareX *11*, 100506. https://doi.org/10.1016/j.softx.2020.100506.

69. Lin, J., and Khoo, E. (2024). Identifiability study of lithium-ion battery capacity fade using degradation mode sensitivity for a minimally and intuitively parametrized electrode-specific cell open-circuit voltage model. J. Power Sources *605*, 234446. https://doi.org/10.1016/j.jpowsour.2024.234446.

70. Lee, S., Siegel, J.B., Stefanopoulou, A.G., Lee, J.W., and Lee, T.K. (2020). Electrode state of health estimation for lithium ion batteries considering half-cell potential change due to aging. J. Electrochem. Soc. *167*, 090531. https://doi.org/10.1149/1945-7111/ab8c83.